Mass Map Reconstruction By Weak Gravitational Lensing

Departmental Project-I

Supriyo Saha
supriyo.saha@tifr.res.in

Supervised by
Dr. Mohamed Rameez

February 8, 2025

Tata Institute of Fundamental Research

Mumbai, India

1 Motivation

In the DES Y3-Year analysis, mass map was created using ellipticity values derived from galaxy shapes. A notable aspect of their analysis was the presence of a non-zero mean shear in the catalog, which was subtracted before constructing the maps. The underlying cause of this non-zero mean shear, however, remains unknown. While the DES analysis team did not mention any reason .

In this work, I have successfully reproduced the DES mass map. I aim to analyze the origin and implications of the observed mean shear in the future. This analysis could provide deeper insights into the potential sources of anisotropy in the data and their impact on cosmological measurements.

2 INTRODUCTION

Gravitational lensing is the bending of light as it passes through the gravitational field of a massive object, such as a galaxy, galaxy cluster, or dark matter halo, due to the curvature of spacetime described by Einstein's General Theory of Relativity.

Figure 1: Galaxy cluster SDSS J1038+4849 and Einstein ring. Credit: NASA/ESA[2]

Gravitational lensing is categorized into three regimes: **strong lensing**, **weak lensing**, and **microlensing**. **Strong lensing** results in prominent phenomena such as Einstein rings, arcs, and multiple images, typically observed in massive galaxy clusters where the alignment between the source, lens, and observer is near-perfect. **Weak lensing** causes subtle statistical distortions in background galaxy shapes. We can infer the underlying mass distribution, including dark matter, from the shear field. From this measurements we can test the cosmological models and constrain dark energy. **Microlensing** occurs when a massive object (lens) passes in front of a background source, temporarily magnifying its light without creating multiple images. It involves lower-mass lenses and is monitored over time through changes in brightness, shown as a light curve.

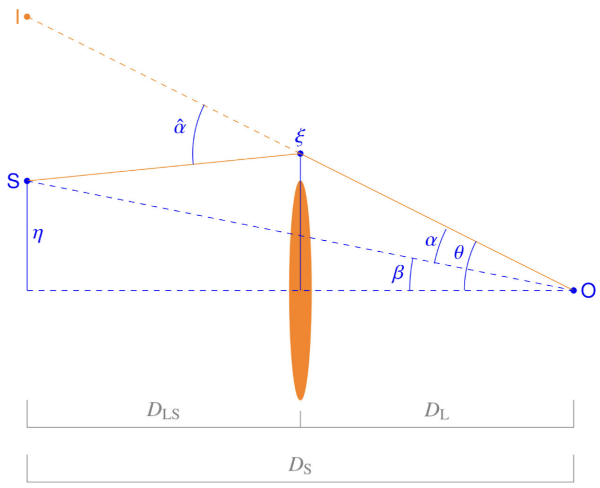

Figure 2: Schematic diagram illustrating the simple Newtonian approach to gravitational lensing.(adapted from Narayan and Bartelmann [14]).

3 Deflection of Light

The idea that gravity could bend the trajectory of light rays originated before the formulation General relativity. We can compute the bending of trajectory of massless light particles due to massive objects using standard newtonian physics.

The deflection angle can be written as

$$\hat{\alpha}_{Newtonian} = \frac{2MG}{c^2 b} \tag{1}$$

where, M is mass of the lensing object, G is Gravitational constant, c is Speed of light, b is Impact parameter. However,in 1919 Edington showed that the prediction was incorrect by a factor 2 compare to Einstein's theory.

From General Relativity calculations, we can show that the deflection angle (see Bartelmann and Maturi [1]) is given by:

$$\alpha = \frac{2}{c^2} \int_{s_A}^{s_B} \vec{\nabla}_{\perp} \Phi \, ds$$

3.1 Light Deflection in the FLRW Universe

In the FLRW metric with spherical coordinates (ct, χ, θ, ϕ), the transverse comoving separation between two light rays, in the absence of perturbations, is given by:

$$x_0(\chi) = f_K(\chi)\theta,$$

where $f_K(\chi)$ is the comoving angular diameter distance, and θ is the observed angular separation. Gravitational lensing introduces perturbations due to the lensing potential Φ, modifying the separation between rays. The induced change in the separation vector at a source located at comoving distance χ is expressed as:

$$x(\chi) = f_K(\chi)\theta - \frac{2}{c^2} \int_0^{\chi} f_K(\chi - \chi_0) \nabla_{\perp} \Phi(x, \chi_0) d\chi_0.$$

The observed angle θ and the unperturbed source position β are related via the lens equation:

$$\beta = \theta - \alpha, \tag{2}$$

we can write the deflection angle as α is:

$$\alpha = \frac{2}{c^2} \int_0^{\chi} \frac{f_K(\chi - \chi_0)}{f_K(\chi)} \nabla_\perp \Phi(x, \chi_0) d\chi_0.$$

The gravitation potential,Φ projected along the line of sight can be written as

$$\Phi(\chi, \theta, \phi) = \frac{2}{c^2} \int_0^{\chi} d\chi_0 \frac{f_K(\chi - \chi_0)}{f_K(\chi) f_K(\chi_0)} \Phi(\chi_0, \theta, \phi)$$

Instead of doing this three dimensional analysis we we integrate it over the redshift distribution n(z) of source galaxies to marginalize the radial dependance.

$$\Phi(\theta, \phi) = \int d\chi \, n(z(\chi)) \, \Phi(\chi, \theta, \phi)$$

3.2 Convergence and Shear

We define the inverse amplification matrix $A = \partial\vec{\beta}/\partial\vec{\theta}$. From equation (2)we can write

$$A_{ij} = \frac{\partial \beta_i}{\partial \theta_j} = \delta_{ij} - \frac{\partial \alpha_i}{\partial \theta_j} = \delta_{ij} - \frac{\partial^2}{\partial x_i \partial x_j} \Phi(\theta, \chi)$$

The amplification matrix **A** is compactly represented in terms of the convergence κ and the complex shear field $\gamma = \gamma_1 + i\gamma_2$ as:

$$\mathbf{A} = \begin{pmatrix} 1 - \kappa - \gamma_1 & -\gamma_2 \\ -\gamma_2 & 1 - \kappa + \gamma_1 \end{pmatrix}. \tag{3}$$

The convergence κ and the shear components γ_1, γ_2 are evaluated at a given spacetime position (θ, x) and are derived from the lensing potential ψ as:

$$\kappa = \frac{1}{2}(\partial_i \partial_i + \partial_j \partial_j)\Phi, \tag{4}$$

$$\gamma_1 = \frac{1}{2}(\partial_i \partial_i - \partial_j \partial_j)\Phi, \tag{5}$$

$$\gamma_2 = \partial_i \partial_j \Phi. \tag{6}$$

Here, the shear field γ is a spin-2 quantity whose amplitude quantifies the distortion magnitude, while its phase determines the direction of distortion.

Convergence from Shear Field

There are many methods for generating the convergence field from the shear field. One of the popular methods is the Kaiser & Squires direct inversion method (Kaiser and Squires [11]).

Spherical Kaiser-Squires (SKS) formalism

The Spherical Kaiser-Squires (SKS) formalism is an extension of the flat-sky approach developed by Kaiser and Squires [11] to analyze weak lensing on the spherical sky.

The lensing potential $\phi(r)$ can be expanded in spherical harmonics $Y_{lm}(\theta, \phi)$ as follows:

$$\phi(r) = \sum_{l=0}^{\infty} \sum_{m=-l}^{l} \phi_{lm} Y_{lm}(\theta, \phi),$$

where ϕ_{lm} are the spherical harmonic coefficients, and $Y_{lm}(\theta, \phi)$ are the spherical harmonics.

The shear field in spherical space can be written as:

$$\gamma(r) = \sum_{l=0}^{\infty} \sum_{m=-l}^{l} \hat{\gamma}_{lm} \, {}_{\pm 2}Y_{lm}(\theta, \phi),$$

The convergence field κ is a scalar field and is therefore expanded using spin-0 spherical harmonics ${}_0Y_{lm}(\theta, \phi)$. The convergence field is written as:

$$\kappa(r) = \sum_{l=0}^{\infty} \sum_{m=-l}^{l} \hat{\kappa}_{lm} \, {}_0Y_{lm}(\theta, \phi).$$

The harmonic space relations between κ, γ, and Φ are (see Jeffrey et al. [10]):

$$\kappa_{\ell m} = -\frac{1}{2}\ell(\ell+1)\Phi_{\ell m}, \quad \gamma_{\ell m} = \frac{1}{2}\sqrt{(\ell-1)\ell(\ell+1)(\ell+2)}\Phi_{\ell m}.$$

The shear coefficients $\hat{\gamma}_{lm}$ and the convergence coefficients $\hat{\kappa}_{lm}$ are related by equation(see Castro et al. [4],Kansal [12]):

$$\hat{\gamma}_{lm} = -\sqrt{\frac{(l+2)(l-1)}{l(l+1)}}(\hat{\kappa}_{E,lm} + \hat{\kappa}_{B,lm}) = S_l \hat{\kappa}_{lm} \tag{7}$$

where the factor $\sqrt{\frac{(l+2)(l-1)}{l(l+1)}}$ is denoted as S_l. This relation defines the spherical analog of the Kaiser & Squires method for weak lensing, establishing the relation between the shear and convergence fields in spherical space. In the flat-sky approximation, the decomposition into spherical harmonics is replaced by a Fourier transform:

$$\sum_{l,m} \phi_{lm} Y_{lm} \rightarrow \int \frac{d^2 l}{(2\pi)^2} \phi(l) e^{i\mathbf{l}\cdot\boldsymbol{\theta}},$$

which reduces the equations to the standard Kaiser & Squires (1993) formalism. This mapping is referred to as the Spherical Kaiser-Squires (SKS) method.

However, this method can be noisy, especially in regions with low signal-to-noise ratio, as it directly inverts the shear field without smoothing. To address this issue, a smoothing technique is often applied to reduce the noise in the reconstructed convergence field.

4 The Dark Energy Survey

The Dark Energy Survey (DES) is an international collaboration designed to observe the accelerating expansion of the universe and help understand the nature of dark energy. The survey involved over 400 scientists from over 25 institutions globally. The collaboration built 570-megapixel DECam (Flaugher et al. 2015), a highly sensitive digital camera installed at the prime focus of the 4-meter Blanco Telescope at Cerro Tololo Inter-American Observatory (CTIO) in Chile (see Fig. 3).

4.1 Dark Energy Camera (DECam)

DECam consists of five large optical lenses, a Hexapod alignment system, a shutter, color filters (spanning 400–1080 nm), and a digital imager. The DECam system comprises 74 CCDs (charge-coupled devices) operating across five optical and near-infrared broadbands (grizY). DECam captures wide-field images with a readout time under 30 seconds. Construction began in 2008, with installation completed in 2012.DECam successfully identified and measured the position, morphology, and photometric redshifts of approximately 300 million galaxies, 3000 type Ia supernovae, and tens of thousands of galaxy clusters.

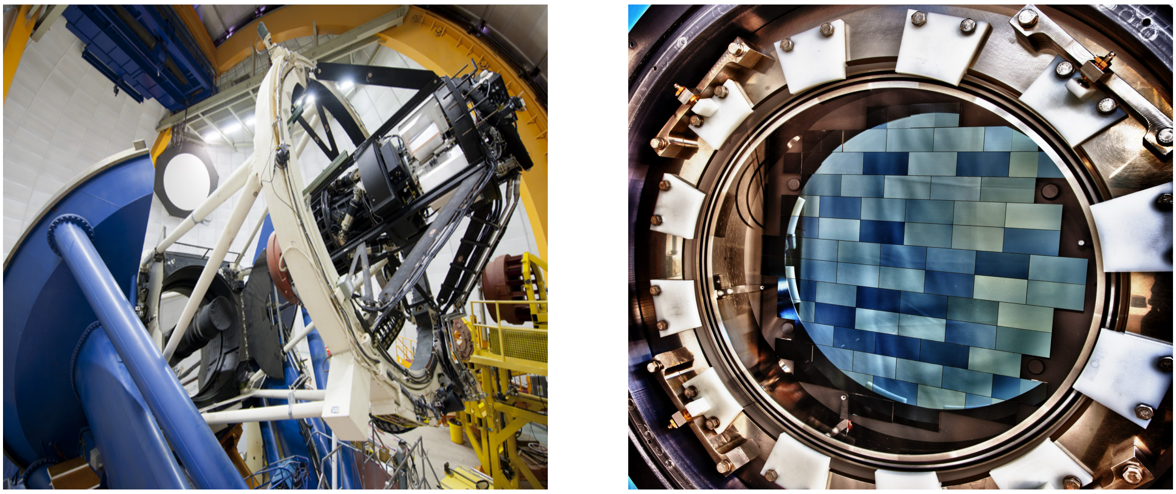

Figure 3: Blanco Telescope with DECam installed (left) and DECam imager with CCDs (blue) in place (right). Image credit: Dark Energy Survey (DES).

4.2 Dataset: Y3 Cosmology Data

I have used the DES Y3 data products for my analysis.The catalog files can be found in this directory.The catalogs are all linked within the index file, allowing access to the data directly in Python using tools such as h5py by loading only the index file. For this to function correctly, all catalog files must be located in the same directory.In this github repository https://github.com/des-science/DESY3Cats, they have provided how to interact with the HDF5 catalog files linked to DES that were used internally. We can directly calculate shear response function automatically from these classes.

4.3 Shear Catalogue

The shear catalogue is fully described detailly in Gatti et al. [6],based on the Y3 Gold catalogue (Sevilla-Noarbe et al. 2020). It is constructed using the METACALIBRATION algorithm (Huff and Mandelbaum [9]; Sheldon and Huff [15]), which estimates galaxy ellipticities from images in the r, i, and z bands. The shear catalogue is divided into four tomographic bins, with redshift distributions ($n(z)$) estimated using the SOMPZ method (Myles et al. 2020) .

5 Shear Estimation

One of the main objective of weak lensing is to correct the estimate of the shear field.As the true shape of the galaxies are not observable, measurement of galaxy shapes is a very complex task.To reduce the shape noise a large number of galaxies must be measured. Here, we will outline the pipeline used for the DES Y3 analysis:

5.1 Detection of Object:

In object detection, sources are identified by finding peaks above a set threshold (e.g., Source Extractor, Bertin and Arnouts [3]). Each sky patch is observed multiple times by DECam, and the individual single-epoch images are combined through a weighted average to enhance the overall signal-to-noise ratio (S/N) and minimize the influence of transient artifacts.

5.2 PSF Modeling

After object detection, the image must be deconvolved with the Point Spread Function (PSF), which characterizes how an imaging system responds to a point source. Accurate PSF modeling is essential for recovering the true image and is typically calibrated using stars.In the DES Y3 analysis, the Point Spread Function (PSF) is estimated using an empirical approach.

5.3 Metacalibration

In the DES Y3 analysis, the shear estimation was carried out using the METACALIBRATION algorithm (Huff and Mandelbaum [9],Sheldon and Huff [15]), which performs self-calibration of the shear measurement by manipulating real images.

Suppose we have a noisy ,baised measurement e representing the shear estimate, where $e = (e_1, e_2)$ is the two-component ellipticity of an object. This estimator can be expanded in a Taylor series for small shear as follows:

$$e = e\Big|_{\gamma=0} + \frac{\partial e}{\partial \gamma}\Big|_{\gamma=0}\gamma + \dots$$

where $e_{\gamma=0}$ represents the ellipticity at zero shear, and R is the shear response:

$$R_\gamma \equiv \frac{\partial e}{\partial \gamma}\Big|_{\gamma=0}$$

The derivative is taken with respect to the two-component shear γ, making R_γ a 2×2 matrix:

$$R = \begin{pmatrix} \frac{\partial e_1}{\partial \gamma_1} & \frac{\partial e_2}{\partial \gamma_1} \\ \frac{\partial e_1}{\partial \gamma_2} & \frac{\partial e_2}{\partial \gamma_2} \end{pmatrix}.$$

Assuming the shear is small, we can neglect terms of order γ^2 and higher , so the ensemble mean of $\mathbf{e}$ can be written as :

$$\langle e \rangle \approx \langle e \rangle \Big|_{\gamma=0} + \langle R_\gamma \gamma \rangle \approx \langle R_\gamma \gamma \rangle$$

Given a set of measurements $\{e_i\}$ and corresponding responses $\{R_{\gamma_i}\}$, we can compute unbiased estimates of the shear γ. For instance, to estimate the mean shear γ_{est}, we can express it as:

$$\langle \gamma_{\text{est}} \rangle \approx \langle R_\gamma \rangle^{-1} \langle e \rangle$$

The shear estimate γ_{est} is calculated as a weighted average of the measured e, with weights R_γ.

The shear response matrix R_γ is measured using finite difference derivatives. This is done by applying small shear values ($\pm\gamma \sim 0.01$) to the image and calculating the difference in ellipticity measurements e between the sheared images:

$$R_{\gamma_{i,j}} = \frac{e_i^+ - e_i^-}{\Delta \gamma_j}$$

where $e_i^\pm$ represents the i-th component of the ellipticities measured from images that have been sheared by an artificial shear, with the j-th component of the shear set to $\pm\gamma$.

To perform the shearing, the image is deconvolved by the PSF, sheared, and then reconvolved with the PSF. Since the reconvolution produces a different PSF, ellipticity measurements must be made on the reconvolved but unsheared image (Sheldon and Huff [15]).

Shear responses in DES are typically $R_\gamma \approx 0.6$, varying with factors such as signal-to-noise ratio and object size relative to the PSF. Selection effects, typically a few percent, also influence the shear estimate. These effects can be accounted for by calculating a new ensemble response $\langle R_s \rangle$ based on sheared measurements (Sheldon & Huff 2017). The total response matrix is given by

$$\langle R \rangle = \langle R_\gamma \rangle + \langle R_s \rangle,$$

and shear estimates are computed using:

$$\langle \gamma_{\text{est}} \rangle = \langle R \rangle^{-1} \langle e \rangle. \tag{8}$$

The response matrix $\langle R \rangle$ is approximately diagonal, simplifying the correction to element-wise division.

Despite self-calibration, small multiplicative and additive biases remain due to PSF misestimation and blending. These biases are represented as:

$$\gamma_{\text{est}} = m_i \gamma_{\text{true}} + c_i$$

where m_i and c_i are the multiplicative and additive biases, respectively. PSF misestimation contributes both biases, while blending introduces a multiplicative bias of approximately 2-3%. Additive biases are identified through null tests, and multiplicative biases are quantified using simulations with known shear values.

6 Analysis

I have reconstructed a weak lensing convergence map (mass map) from the observed shear field using the catalog described in Section 4.2. The detailed procedure for calculating convergence values from galaxy ellipticities is presented below.

6.1 Object Selection criteria in DES Y3 Shear Measurements

The DES Y3 shear analysis applied the following selection criteria for weak lensing objects Gatti et al. [6]:

- **Signal-to-Noise Ratio (S/N):** $10 < \text{S/N} < 1000$ to exclude faint objects prone to detection biases and bright objects with large noise fluctuations (Zuntz et al. [16]).
- **Galaxy to PSF Size Ratio:** $T/T_{\text{PSF}} > 0.5$ to mitigate PSF modeling errors.
- **Size Constraints:** $T < 10\,\text{arcsec}^2$ and $T > 2\,\text{arcsec}^2$ with $\text{S/N} < 30$ to remove faint, large blends.
- **Photometric Redshift:** Objects were restricted to $18 < i < 23.5$, $15 < r, z < 26$, and $-1.5 < r - z < 4$ to ensure reliable redshifts (Myles et al. 13).
- **Binary Star Contamination:** High-ellipticity objects ($|\mathbf{e}| > 0.8$) were excluded using $\log_{10}(T) < (22.5 - r)/2.5$ (Hildebrandt et al. 2017).

These selections minimize shear-dependent biases, corrected via the selection response term, R_s. The total number of selected objects is 100,204,026.

I did not directly implement the selection criteria in my code . Instead, I used the code uploaded in the GitHub repository mentioned in Section 4.2 to extract the data with masking. The mask is defined in the index catalog, and the code is used to obtain the data directly after applying the mask.

6.2 Shear field estimation

Shear maps are generated using HEALPix pixelization (Gorski et al. [7]) with $NSIDE =$ 1024, corresponding to a pixel size of 3.44 arcmin. The shear field in each pixel is calculated as:

$$\gamma^{\nu}_{\text{obs}} = \frac{\sum_{j=1}^{n} \epsilon^{\nu}_{j} w_j}{\overline{R} \sum_{j=1}^{n} w_j}$$

where ν represents the two shear components, n is the number of galaxies, w_j is the inverse variance weight, and $\overline{R}$ is the average METACALIBRATION response. The shear maps are constructed for the full catalogue and each tomographic bin.The catalog has a non-zero mean shear with an unknown origin, which is removed at the catalog level before performing any analysis.

6.3 Inverse Variance weight and Number density

When estimating a shear signal from a set of galaxies, not all galaxies contribute equally to the measurement's accuracy. Differences in factors like signal-to-noise ratio (S/N), intrinsic shape noise, and measurement noise cause some galaxies to have more uncertain shape measurements than others. To account for this, we assign a weight w_i to each galaxy, where the weight is proportional to the inverse of the variance of its shear estimated.

from Eq. (8) we can write

$$\sigma_\gamma^2 = \sigma_e^2 \langle R \rangle^{-2}$$

Now the weight is defined as

$$w^i = \sigma_\gamma^{-2} = \sigma_e^{-2} \langle R \rangle^2$$

with

$$\sigma_e^2 = \frac{1}{2} \left[\frac{\sum (e_{i,1})^2}{n_{\text{gal}}^2} + \frac{\sum (e_{i,2})^2}{n_{\text{gal}}^2} \right]$$

here n_{gal} is number count in a given bin of galaxies. The effective number density, as defined by (Heymans et al. [8]), is given in terms of the shear weight w_i for each galaxy as:

$$n_{\text{eff}} = \frac{1}{A} \frac{\left(\sum w_i\right)^2}{\sum w_i^2},$$

where A is the survey area. The corresponding shape variance is defined as:

$$\sigma_e^2 = \frac{1}{2} \left[\frac{\sum (w_i e_{i,1})^2}{\left(\sum w_i\right)^2} + \frac{\sum (w_i e_{i,2})^2}{\left(\sum w_i\right)^2} \right] \left[\frac{\left(\sum w_i\right)^2}{\sum w_i^2} \right],$$

where $e_{i,1}$ and $e_{i,2}$ are the components of ellipticity for individual galaxies. For a comparison, the definition of effective number density provided by Chang et al. [5] can also be used but is not explicitly shown here.

The spatial distribution of the effective number density n_{eff} and the shape variance σ_e are shown in Fig. 4

6.4 Map Reconstruction

In weak lensing, the observed ellipticity of a galaxy, ϵ_{obs}, is related to the reduced shear g and the intrinsic ellipticity of the source galaxy, ϵ_s, by:

$$\epsilon_{\text{obs}} \approx g + \epsilon_s$$

where the reduced shear is:

$$g = \frac{\gamma}{1 - \kappa}$$

In the weak lensing limit, $g \approx \gamma$.

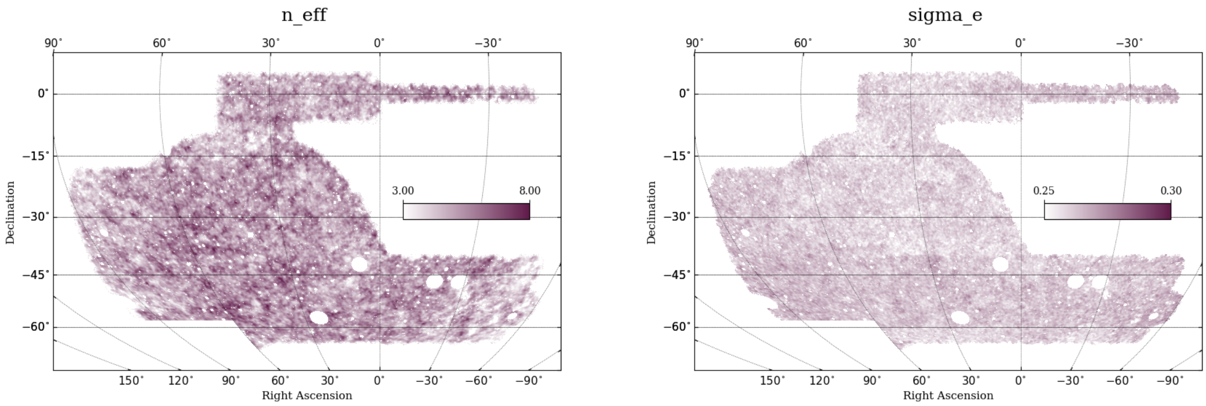

Figure 4: Maps showing the effective number density (n_{eff}) and shape variance (σ_e) across the survey area.

$$\gamma_{\text{obs}} \approx \gamma + \epsilon_s$$

We can now calculate the $\hat{\kappa}_{lm}$ from $\hat{\gamma}_{lm}$ in harmonic space using Eq. (7). The Kaiser-Squires method on the sphere applies a spin transformation to the shear maps γ (specifically γ_E and γ_B) to generate both the curl-free E-mode convergence map κ_E, which carries the majority of the cosmological signal, and the divergence-free B-mode convergence map κ_B, which arises due to non-linear lensing effects. The HEALPix function `map2alm` is used to decompose the real-space shear maps (γ_E and γ_B) into spherical harmonic space ($\hat{\gamma}_{\text{obs},E,lm}$ and $\hat{\gamma}_{\text{obs},B,lm}$), as shown in Eq. (7). This can be rewritten as:

$$\hat{\kappa}_n^{lm} = MS_l^{-1}\hat{\gamma}_n^{lm} = S_l^{-1}\hat{\gamma}_{\text{obs}}^{lm}\hat{\kappa}_n^{lm} = MS_l^{-1}\hat{\gamma}_n^{lm} = S_l^{-1}\hat{\gamma}_{\text{obs}}^{lm}$$

Then, the `alm2map` function transforms the spherical harmonic coefficients ($\hat{\kappa}_n^{E,lm}$ and $\hat{\kappa}_n^{B,lm}$) back into real-space maps (κ_E and κ_B). However, since this method does not account for noise and survey masks in the shear fields, the resulting maps can be significantly affected by these factors, leading to poor results. The implementation of the entire reconstruction process, including handling spherical harmonic transformations, is available in this GitHub repository

7 Convergence map(Mass map)

In Fig. 5, the convergence map generated using the Kaiser-Squires (KS) algorithm is shown. This map represents the mass distribution reconstructed from weak lensing data, as part of the DES Y3 analysis. The map has been smoothed with a 10 arcminute Gaussian filter to reduce the noise.

The map shown in Fig. 5 illustrates the convergence (κ) across the sky, where the density fluctuations due to dark matter and other cosmic structures are captured. The Kaiser-Squires algorithm is employed to separate the E-mode and B-mode contributions, which correspond to the curl-free and divergence-free components of the convergence, respectively. The smoothing applied helps to suppress high-frequency noise and highlight the underlying mass distribution.

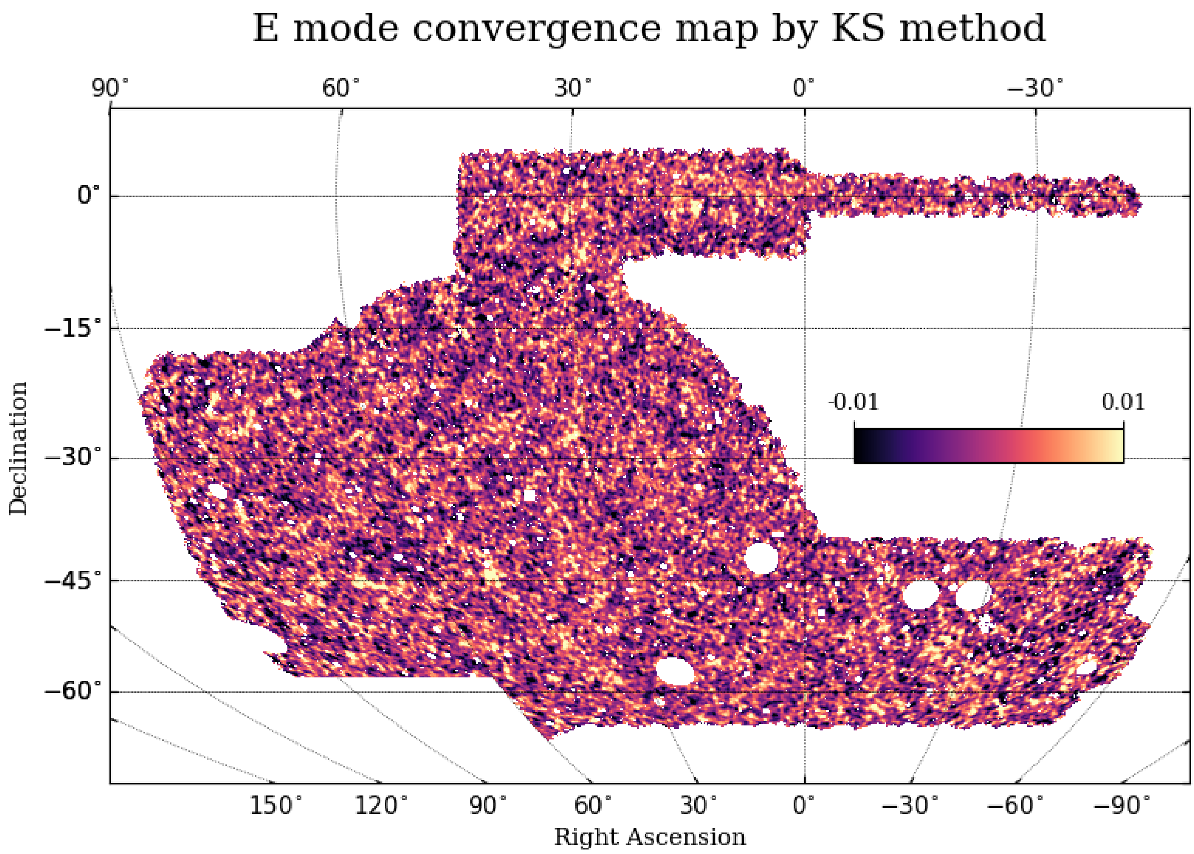

Figure 5: DES Y3 mass map reconstructed using the Kaiser-Squires (KS) algorithm. The map has been smoothed with a 10 arcminute filter.

The reconstructed convergence map provides insight into the cosmic structures, such as clusters and voids, and serves as an important tool for understanding the large-scale structure of the universe.

Acknowledgements

I would like to thank my supervisor, Dr. Mohamed Rameez, for his guidance and support throughout this project. I am also grateful to my seniors, Animesh Sah , Harsh Mehta and Ashish Narayan for their help and for patiently explaining various topics and code realted problems. Their support has been invaluable to me.

References

[1] Matthias Bartelmann and Matteo Maturi. Weak gravitational lensing, 2016. URL https://arxiv.org/abs/1612.06535.

[2] V. Belokurov, N. W. Evans, P. C. Hewett, A. Moiseev, R. G. McMahon, S. F. Sanchez, and L. J. King. Two new large-separation gravitational lenses from sdss. *Monthly Notices of the Royal Astronomical Society*, 392 (1):104–112, January 2009. ISSN 1365-2966. doi: 10.1111/j.1365-2966.2008.14075.x. URL http://dx.doi.org/10.1111/j.1365-2966.2008.14075.x.

[3] E. Bertin and S. Arnouts. SExtractor: Software for source extraction. , 117:393–404, June 1996. doi: 10.1051/aas:1996164.

[4] P. G. Castro, A. F. Heavens, and T. D. Kitching. Weak lensing analysis in three dimensions. *Physical Review D*, 72(2), July 2005. ISSN 1550-2368. doi: 10.1103/physrevd.72.023516. URL http://dx.doi.org/10.1103/PhysRevD.72.023516.

[5] C. Chang, M. Jarvis, B. Jain, S. M. Kahn, D. Kirkby, A. Connolly, S. Krughoff, E.-H. Peng, and J. R. Peterson. The effective number density of galaxies for weak lensing measurements in the lsst project. *Monthly Notices of the Royal Astronomical Society*, 434 (3):2121–2135, July 2013. ISSN 1365-2966. doi: 10.1093/mnras/stt1156. URL http://dx.doi.org/10.1093/mnras/stt1156.

[6] M. Gatti et al. Dark energy survey year 3 results: weak lensing shape catalogue. *Mon. Not. Roy. Astron. Soc.*, 504(3):4312–4336, 2021. doi: 10.1093/mnras/stab918.

[7] K. M. Gorski, E. Hivon, A. J. Banday, B. D. Wandelt, F. K. Hansen, M. Reinecke, and M. Bartelmann. Healpix: A framework for high-resolution discretization and fast analysis of data distributed on the sphere. *The Astrophysical Journal*, 622(2):759–771, April 2005. ISSN 1538-4357. doi: 10.1086/427976. URL http://dx.doi.org/10.1086/427976.

[8] Catherine Heymans, Ludovic Van Waerbeke, Lance Miller, Thomas Erben, Hendrik Hildebrandt, Henk Hoekstra, Thomas D. Kitching, Yannick Mellier, Patrick Simon, Christopher Bonnett, Jean Coupon, Liping Fu, Joachim Harnois Déraps, Michael J. Hudson, Martin Kilbinger, Koenraad Kuijken, Barnaby Rowe, Tim Schrabback, Elisabetta Semboloni, Edo van Uitert, Sanaz Vafaei, and Malin Velander. CFHTLenS: the Canada-France-Hawaii Telescope Lensing Survey. , 427(1): 146–166, November 2012. doi: 10.1111/j.1365-2966.2012.21952.x.

[9] Eric Huff and Rachel Mandelbaum. Metacalibration: Direct self-calibration of biases in shear measurement, 2017. URL https://arxiv.org/abs/1702.02600.

[10] N. Jeffrey et al. Dark Energy Survey Year 3 results: Curved-sky weak lensing mass map reconstruction. *Mon. Not. Roy. Astron. Soc.*, 505(3):4626–4645, 2021. doi: 10.1093/mnras/stab1495. URL https://doi.org/10.1093/mnras/stab1495.

[11] Nick Kaiser and Gordon Squires. Mapping the Dark Matter with Weak Gravitational Lensing. , 404:441, February 1993. doi: 10.1086/172297.

[12] Vanshika Kansal. Reconstruction of weak lensing mass maps for non-gaussian studies in the celestial sphere. *Astronomy amp; Astrophysics*, 670:A34, February 2023. ISSN 1432-0746. doi: 10.1051/0004-6361/202245198. URL http://dx.doi.org/10.1051/0004-6361/202245198.

[13] J. Myles et al. Dark Energy Survey Year 3 results: redshift calibration of the weak lensing source galaxies. *Mon. Not. Roy. Astron. Soc.*, 505(3):4249–4277, 2021. doi: 10.1093/mnras/stab1515.

[14] R. Narayan and M. Bartelmann. Gravitational lensing. In Avishai Dekel and Jeremiah P. Ostriker, editors, *Formation of Structure in the Universe*, page 360, April 1999.

[15] Erin S. Sheldon and Eric M. Huff. Practical weak-lensing shear measurement with metacalibration. *The Astrophysical Journal*, 841 (1):24, May 2017. ISSN 1538-4357. doi: 10.3847/1538-4357/aa704b. URL http://dx.doi.org/10.3847/1538-4357/aa704b.

[16] J. Zuntz et al. Dark Energy Survey Year 1 Results: Weak Lensing Shape Catalogues. *Mon. Not. Roy. Astron. Soc.*, 481(1):1149–1182, 2018. doi: 10.1093/mnras/sty2219.